npj | biological physics and mechanics

Article

https://doi.org/10.1038/s44341-024-00002-2

Hybrid model of tumor growth, angiogenesis and immune response yields strategies to improve antiangiogenic therapy

Andreas G. Hadjigeorgiou & Triantafyllos Stylianopoulos ✉

Solid tumors harbor a complex and dynamic microenvironment that hinders the delivery and efficacy of therapeutic interventions. In this study, we developed and utilized a hybrid, discrete-continuous mathematical model to explore the interplay between solid tumor growth, immune response, tumor-induced angiogenesis, and antiangiogenic drugs. By integrating published data with anti-angiogenic drugs, we elucidate three primary mechanisms by which anti-angiogenesis influences tumor progression and treatment outcomes: reduction in tumor growth rate by mitigating and temporally delaying angiogenesis, normalization of blood vessel structure and function, and improving immune cell extravasation and activation. Our results indicate a significant increase in functional blood vessels and perfusion following anti-angiogenic treatment, which in turn improves the intratumoral distribution of immune cells. The normalization window, or optimal time frame for anti-angiogenic drug administration, and the dose of the drug arise naturally in the model and are highlighted as crucial factors in maximizing treatment benefits. Prolonged anti-angiogenic treatment triggers cancer cell migration into healthy tissue and induces immunosuppression due to hypoxia, potentially leading to negative effects because these cancer cells will rapidly proliferate upon treatment termination. In conclusion, the positive contribution of anti-angiogenic treatment must balance the possible negative effects by choosing a proper treatment protocol as well as combining it with proper anti-cancer treatment. Our findings provide valuable insights and a framework for the design of protocols with anti-angiogenic treatment, targeted immunotherapy, and non-targeted anti-cancer therapies.

Blood vessels that supply tissues with nutrients and oxygen cannot meet the high demands of rapidly proliferating cancer cells during solid tumor progression, resulting in hypoxia and increased production of angiogenic factors. This increased demand for oxygen is met by the sprouting of new blood vessels from existing ones, a process known as tumor-induced angiogenesis[1]. Cancer cells under hypoxic conditions, over-express tumor angiogenic factors, with the most common being the vascular endothelial growth factor (VEGF) that induces the formation of new vessels. These neo-vessels, however, have abnormal structures and are often over-leaky due to their rapid formation and immaturity, which renders them dysfunctional and not well-perfused[1]. This abnormality of the tumor vasculature contributes to hypo-perfusion, which in turn results in immunosuppression and limited transport of drugs and immune cells into the tumor[1,2]. Therefore, the tumor vasculature plays a crucial role in solid tumor initiation, growth, immune evasion, and response to therapies[3]. Normalization of the tumor vessels with anti-angiogenic drugs (e.g., anti-VEGF antibodies) is a clinically applied treatment to restore the structural abnormalities of the vessels and thus, improve tumor perfusion, oxygenation, and vascular function[4–6]. However, it is still unclear which patients will benefit from such treatments. To provide a mechanistic insight into the effects of anti-angiogenic treatment on tumor progression and immune cell behavior, we developed a mathematical model to investigate the interplay of tumor growth, angiogenesis, anti-angiogenic drugs, and the immune system.

Cancer Biophysics Laboratory, Department of Mechanical and Manufacturing Engineering, University of Cyprus, Nicosia, Cyprus.
✉e-mail: tstylian@ucy.ac.cy

Numerous models have contributed to our understanding of tumor microenvironment dynamic, particularly emphasizing the intricate interplay between vascular networks, interstitial fluid flow, and drug transport. Early work explored the impact of vascular compliance and leakiness on tumor blood flow patterns, revealing hindered drug delivery in central tumor regions due to non-uniform blood supply and interstitial fluid pressure[7]. Anderson and Chaplain[8] employed a discrete model to simulate angiogenesis, considering endothelial cell motion influenced by angiogenic and matrix macromolecule factors and generating vascular networks resembling solid tumor vasculature. Subsequent studies coupled intravascular and interstitial flows, highlighting the influence of vascular leakiness on systemic flow patterns and tumor microenvironments, potentially contributing to cancer cell metastasis[9]. Additional models coupled tumor growth with angiogenesis, offering insights into the temporal and spatial dynamic of avascular and vascular growth stages[10]. Also, investigations combining in vivo experimental data with discrete vasculature simulations explored the impact of vascular normalization on nanomedicine delivery, revealing size-dependent effects of nanoparticles[11–14]. Furthermore, models employing discrete vascular remodeling over time emphasized the significance of mechanical forces in tumor-induced angiogenesis, highlighting the impact of the treatment timing and vessel wall permeability on the effective delivery of drugs[15–17].

To this end, we built on previous research to develop a hybrid model that accounts for a continuous 3-dimensional tumor growth model, a discrete model of tumor-induced angiogenesis vessel remodeling, and a physiological-based kinetics model that simulates the immune cells transport and anti-tumor immune response. The current framework extends previous research by incorporating a detailed model of immune response and anti-tumor immunity that involves also the transport of immune cells and cytokines among the upper and lower trunk, the lymph and blood circulation, as well as the growth of a solid tumor (Fig. 1 and Supplementary information). The model also calculates the perfusion within the vascular network, which allows the quantification of functional vessels that directly affect the infiltration of the immune cells into the tumor. A comparison of the components incorporated in our modeling framework with previously published pertinent models[7–11,13,15–21] is shown in Supplementary Table 1. To our knowledge, the current model is the first to include a non-regular vascular network, vascular flow through the network, interstitial flow, dynamic angiogenesis, tumor growth, and the immune system.

We first compare model predictions and provide mechanistic insights to published experimental data that involved anti-VEGF treatment in a murine glioma model. Then we present model predictions for the effect of the anti-VEGF treatment on vessels' blood velocity, oxygen concentration, and tumor growth, and provide insights into how anti-VEGF treatment can improve blood vessel functionality. Finally, we present the spatiotemporal

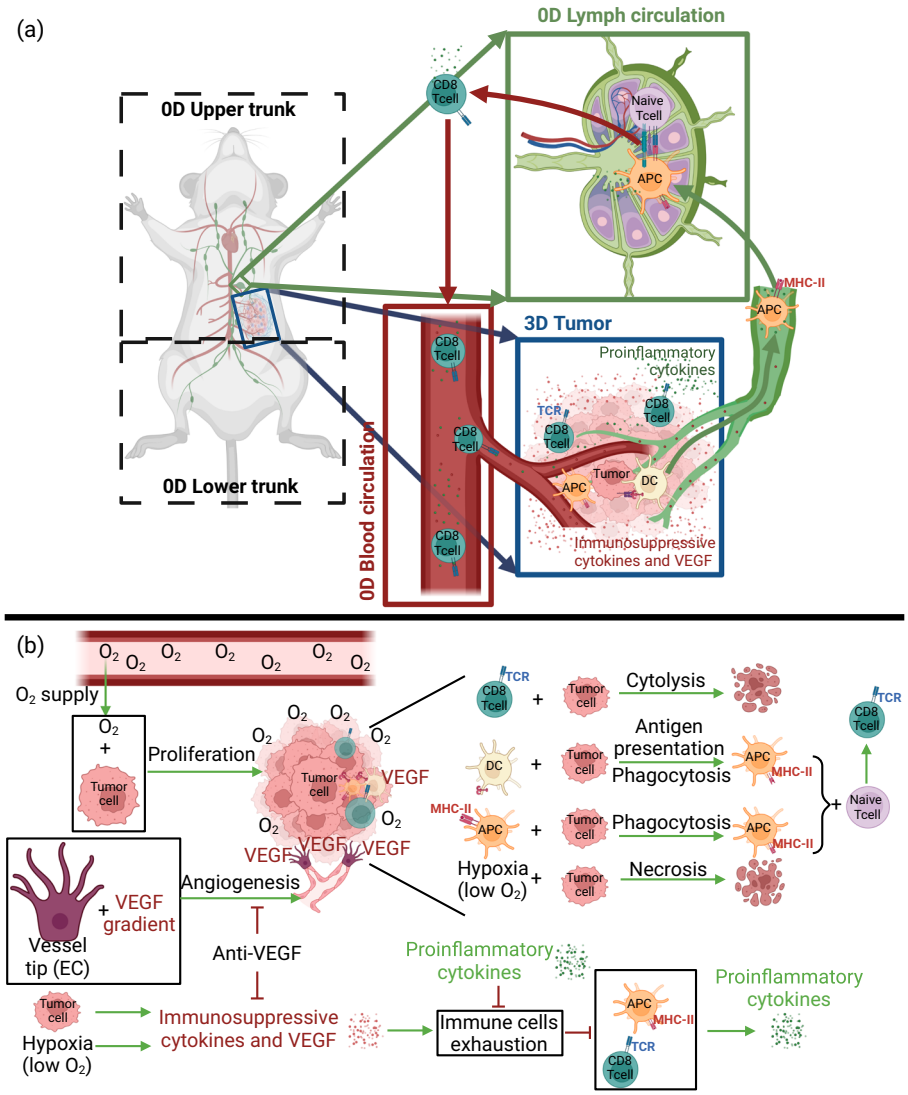

Fig. 1 | Hybrid model of immune-cancer interactions and angiogenesis dynamic. Schematic representation of the model compartments (**a**) and the main interactions of immune cells, cancer cells, cytokines, angiogenesis, anti-angiogenic treatment, and oxygen (**b**). **a** The compartments of the model and the immune cells and cytokines that are circulated through the entire mouse body. The mouse was divided into the following compartments: the tumor, upper trunk, lower trunk, lymph circulation, and blood circulation. The tumor is modeled as a 3D compartment with a spherical geometry, and the rest of the mouse (upper trunk, lower trunk, blood, and lymph circulation) are modeled as homogenous (0D) compartments. All the compartments are connected with blood and lymph circulation and the balance of all variables was kept through all compartments. Dendritic cells, antigen-presenting cells, $CD8^+$ effector T-cells, and cytokines (immunosuppressive and pro-inflammatory) can enter the tumor via the tumor vessels and return back to circulation via the tumor-draining lymphatic vessels. The dendritic cells that are activated to present the tumor antigen can be transported to the lymph node and activate naïve T-cells against the tumor antigen. **b** The oxygen (O_2) as a nutrient is supplied by the blood vessels and fuels the cancer cells proliferation. Hypoxia induces the VEGF production which attracts the nearby vessels to move through the VEGF gradient. Cancer cells induce immunosuppressive cytokines which can induce immune cell exhaustion which can be inhibited by pro-inflammatory cytokines. $CD8^+$ effector T-cells can induce cytolysis in the cancer cells, and dendritic cells (DC) and antigen-presenting cells (APC) can phagocytosis the cancer cells. The antigen-presenting cells activate the naïve T-cells like $CD8^+$ T-cells against tumor antigen ($CD8^+$ effector T-cells). $CD8^+$ effector T-cells and APC produce pro-inflammatory cytokines. Further details are provided in the Supplementary Information. Created with BioRender.com.

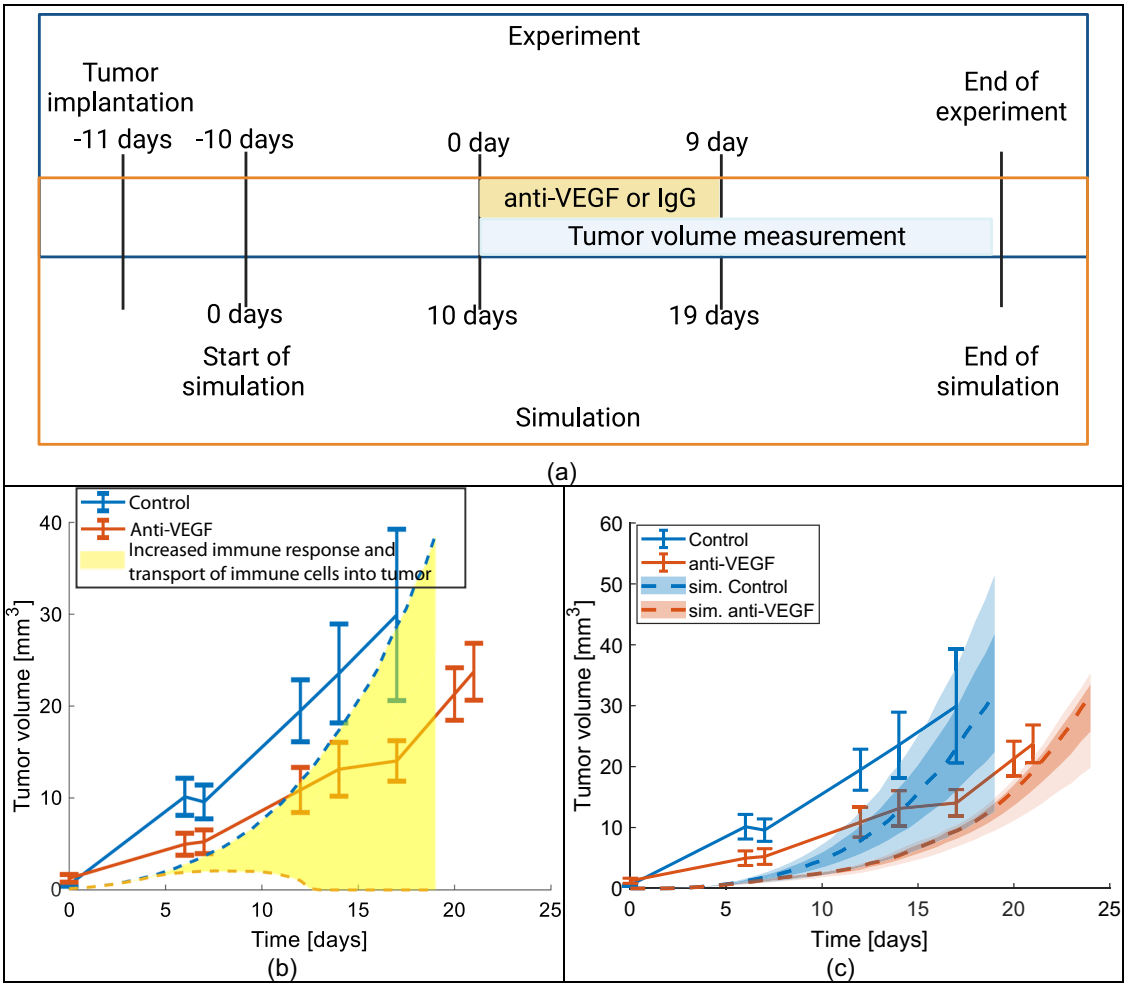

Fig. 2 | Validation of simulation results with anti-VEGF treatment and sensitivity of crucial parameters. a The timeline of the experiment and the simulation (created with BioRender.com). **b** Sensitivity of the model by increasing the immune response (killing potential of immune cells) and the transport (extravasation) of immune cells. **c** Validation of the model, comparison of the simulated (dashed curves) with experimental tumor (continuous curves). The average values of the experimental tumor growth data are presented along with their standard errors. The simulated curves are presented with a range (shaded areas) by varying +−5% and +−2.5% (light-shaded and darker-shaded areas, respectively) the tumor growth rate constant (parameter l_c) and cancer cells' random mobility (i.e., their invasiveness to the surrounding tissue, parameter D_c.) from their baseline values.

distribution of antigen-presenting cells, $CD8^+$ effector T-cells, and pro-inflammatory and immunosuppressive cytokines, following anti-VEGF treatment.

Results

Model validation with experimental data of anti-VEGF therapy

First, we set out to compare model predictions with data from the response of mouse GSC005 glioblastoma to anti-VEGF treatment[4]. Figure 2a presents the experimental and simulated protocols. The simulation starts on day −10 of the experiment, a day after tumor implantation, as the model needs a small finite tumor volume to start with. After day −10 the simulation and the experimental protocol overlap, as shown in Fig. 2a. Anti-VEGF treatment started on day 0 (day 10 of simulation), and the last dose was given on day 9 (day 19 of simulation).

Figure 2b shows the comparison of the experimental tumor growth curves with the model predictions for a baseline immune response and for increasing the model parameters related to the extravasation of immune cells into the tumor and their killing potential. Specifically, the blue dashed line represents the case of a baseline immune response without any vascular normalization. By further increasing the extravasation of the immune cells into the tumor compartment and the killing potential of immune cells (i.e., increased immune response) the tumor can be eliminated (orange dashed line). Given that the experimental tumor volume of the anti-VEGF group is lower than the control group and at the final stages of tumor growth both curves have a similar slope (Fig. 2b), we surmised that the lower tumor volume in the case of anti-VEGF was due to a reversible effect during treatment. The reversible effect of anti-angiogenic treatment could be a transient delay of angiogenesis which causes a reduction of oxygen and nutrient supply and not due to a significant anti-tumor immune response. A robust anti-tumor immune response would persist even after the last dose of anti-VEGF and tumor volume would follow a similar behavior to the orange curve in Fig. 2b, which is the effect of a strong anti-tumor immune response. In the pertinent literature, it is also well established that proper doses of anti-angiogenic treatment can induce vessel normalization, which is defined by the pruning of some immature/dysfunctional vessels and reduction in vessel permeability[18,19]. These changes in tumor vasculature have the potential to improve the efficacy of treatments, such as immunotherapy and/or chemotherapy. However, vascular normalization treatment alone often is not effective[20], which explains the increase in tumor growth after the termination of anti-angiogenic treatment observed in the experimental data in Fig. 2b.

The analysis of the experimental data along with the predictions of the model and the established mechanisms of anti-angiogenic treatments[18,19,21,22] leads us to the following hypotheses: (i) anti-VEGF treatment could mitigate

and temporally delay the angiogenesis and (ii) normalize the vasculature by reducing the permeability of the vessels and/or pruning immature vessels. This in turn would affect overall tumor perfusion and oxygenation. Furthermore, in the experimental data of Fig. 2, vascular normalization with anti-VEGF treatment could affect immune cell infiltration but it cannot lead to a sufficient increase in the immune response in order to cause robust anti-tumor effects (i.e., the immune stimulation by anti-VEGF was not sufficient by itself to significantly reduce tumor volume). To prove our hypotheses and the underlying mechanisms, we set to validate the experimental data with our model by incorporating the necessary mechanisms and the appropriate parameters for these mechanisms. The simulated and experimental curves for each group are presented in Fig. 2c where all the parameters of the immune system, cell extravasation, and tumor growth are the same for both groups, and only the anti-angiogenic treatment changed according to the experiment (for the values of the model parameters see Supplementary Table 2). For the simulated growth curves a range of tumor volumes was calculated by varying by $+-5\%$ and $+-2.5\%$ the tumor growth rate constant and cancer cells' random mobility (i.e., their invasiveness to the surrounding tissue) from their baseline values. These parameters were selected due to their clinical implication in glioblastoma and other cancers. Specifically, more aggressive tumors, such as high-grade glioblastoma, proliferate faster and are more invasive[23–25], and thus, they exhibit a higher tumor growth rate constant and cancer cells' random mobility. These types of cancer cells are also able to shift from a proliferative to an invasive phenotype based on the availability of nutrients/oxygen or space[26,27]. This shifting of phenotypes arises naturally in our model because the tumor growth rate constant and cancer cells' random mobility are parameters that define the maximum proliferation and invasion rates, not the actual rates; the actual rates depend also on the availability of oxygen and space which determine if the invasion or proliferation will prevail.

An improvement in tumor response can be achieved by anti-VEGF monotherapy, but the effect is reversible according to both simulated and experimental tumor curves and it is observed only within the time window of anti-VEGF treatment. The increase in the proliferation and invasion parameters by $+5\%$ or $+2.5\%$ leads to greater tumor volumes of 50 mm^3 and 40 mm^3, respectively (see the upper range of blue-shaded areas in Fig. 2c). The use of anti-VEGF treatment for such cases results in a higher reduction of tumor volume by 30 mm^3 to 40 mm^3 compared to the less proliferative and invasive tumors (-5% or -2.5%), where the reduction in tumor volume ranges from 10 mm^3 to 2 mm^3. Overall, the trend in experimental and simulated curves is in good agreement, which is considered acceptable given the complexity of the biological system. Further improvement of the validation can be achieved by varying extensively the parameters that affect the angiogenesis, the tumor growth, and the immune system which is computationally demanding and will not change the main conclusions for the underlying mechanisms. Because of the large variation in the experimental data of tumor growth, even within the same treatment group, we chose to follow the trend of the data rather than overfit our model by extensively varying all model parameters. Overfitting the experimental data will not improve the predictability of our model, on the other hand, it will capture the random fluctuations in the data. To justify our approach, we also present the individual experimental data points along with the model predictions (Supplementary Fig. 1).

Effect of anti-VEGF treatment on blood vessels' functionality

Next, we investigated the effect of anti-VEGF treatment on blood velocity and distribution of vascular density. The results presented in this section are model predictions from the simulations for control and anti-VEGF treatment (Fig. 2c). We assumed that anti-VEGF not only affects the tumor vasculature by blocking VEGF-induced angiogenesis but also reduces the permeability of the vessels (parameter *Lp*).

Figure 3a, b presents the distributions of the average cross-sectional velocity in the vessels with and without anti-VEGF treatment, and for high and low vessel permeability (*Lp*), respectively, whereas Fig. 4 depicts the spatial representation of the vascular density. The distributions of the average velocity are generated by exploiting the discrete vascular network and intravascular pressures at two different time points (at day 16 and the end of the simulation) and at different regions of the tumor compartment (i.e., peritumoral vs. intratumoral region). Interestingly, all the distributions are shifted to higher blood velocities when the permeability of the vessels is reduced due to anti-VEGF treatment. By comparing the velocity distribution in the intratumoral and peritumoral regions, we infer that it is mostly the intratumoral blood velocity that is affected by anti-VEGF treatment, and the effect is greater at the early stages of the angiogenesis (Fig. 3a, b).

Given that the blood velocity in the vessels determines their functionality, we calculated the percentage of the functional vessels that have a sufficient average cross-sectional velocity greater than 0.1 mm/s[28] for the distributions of Fig. 3a, b. The results for the percent of functional vessels are presented in Table 1 for the entire tumor as well as for the intratumoral and peritumoral regions, with and without anti-VEGF treatment at two time points: on Day 16 and at the end of the simulation. The results show that anti-VEGF increases the percentage of the functional vessels by about 10%, 3%, and 23% for the entire tumor, peritumoral, and intratumoral regions, respectively, on Day 16. These values, however, are reduced significantly until the end of the simulation to 4%, −3 and 10%. This temporal improvement in vessel functionality with anti-VEGF treatment can be explained by the vascular normalization window[14,21,29].

In Fig. 4 the spatial distributions of the entire vessels and the functional vascular density are presented (a) on Day 16 and (b) at the end of the simulation with and without anti-VEGF treatment. Without anti-VEGF (Control), the vascular density always covers a greater volume compared to anti-VEGF treated tumors where the angiogenesis is delayed due to the anti-VEGF treatment. We note also that although on Day 16 the coverage of functional vascular density looks similar, a great proportion of vessels are dysfunctional in control as it is shown in Fig. 3 and Table 1. At the end of the simulation, the difference in the functional vascular density is more pronounced: for control, the functional vessels are localized and randomly spread, whereas for anti-VEGF treatment, the functional vessels are spread more homogeneously inside the tumor.

The effect of anti-VEGF on oxygen concentration and the amount of viable cancer cells in comparison to the control group on day 16 is shown in Fig. 5. The anti-VEGF treatment delays the angiogenesis by reducing the VEGF and this delay affects the oxygen supply which affects the oxygen concentration on the tumor periphery and reduces tumor growth rate. In control, the oxygen concentration is almost uniform, which makes the tumor growth rate independent from oxygen concentration. Finally, anti-VEGF-treated tumors have lower tumor volumes and cancer cells proliferate mostly at the center of the tumor until the termination of anti-VEGF treatment. However, cancer cells migrate in the radial direction inside healthy tissues during anti-VEGF treatment and if vascular normalization is not combined with proper anti-cancer therapy or a sufficient immune response, the cancer cells start to proliferate rapidly after the termination of the anti-angiogenic treatment. The uninhibited collective migration and/or regrowth of tumor cells on the periphery of the tumor can be explained by the "go or grow" mechanism[26,27,30] and the shift of cancer cells from proliferative to invasive and again to proliferative phenotype. The "go or grow" mechanism arises naturally in the current model due to the dependence of cancer cells' growth rate on oxygen concentration and available space (i.e., term $l_c \frac{c_{ox}}{K_{c_{ox}}+c_{ox}} \Phi_c \Phi_f$ which depends on oxygen concentration c_{ox} and fluid volume fraction Φ_f that becomes zero when there is no available space for growth, for more details see the first reaction term of viable cancer cells in Supplementary Table 3).

Spatiotemporal distribution of immune cells and cytokines

Subsequently, we set out to investigate the effect of improved perfusion caused by anti-VEGF treatment on the immune system. An increase in blood velocity (i.e., perfusion) can improve the transport of immune cells to the tumor site, and as more immune cells arrive at the tumor, their infiltration inside the tumor region might be increased. Figure 6 presents the spatial distribution of $CD8^+$ effector T-cells, viable and dead cancer cells for control and anti-VEGF treatment at the end of the simulation. The $CD8^+$

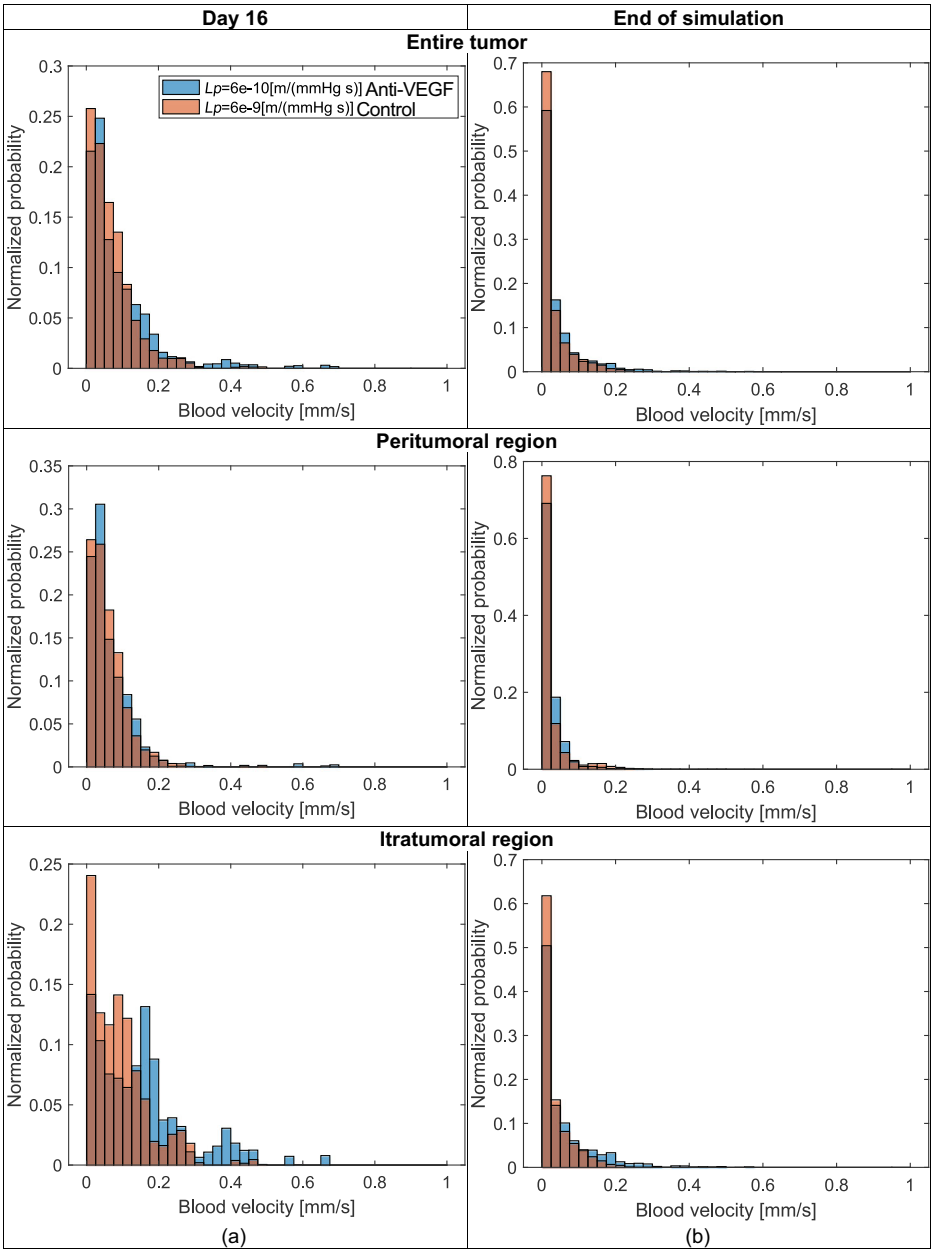

Fig. 3 | Effect of anti-VEGF treatment on blood velocity distribution in tumor vasculature. The distribution of average blood velocity in the vessels with and without anti-VEGF ($Lp = 6\ 10^{-9}$ and $Lp = 6\ 10^{-10}$ [m/(mmHg s)], respectively). **a** on Day 16 and **b** at the end of the simulation. The distributions are shown for different regions of the tumor compartment: entire tumor, peritumoral and intratumoral regions.

effector T-cells are more homogeneously distributed for the anti-VEGF treated tumors compared to the control group, presumably due to improved perfusion (Fig. 4). The anti-VEGF treatment has the highest volume fraction of $CD8^+$ effector T-cells at the center of the tumor. On the contrary, untreated tumors have a high-volume fraction of $CD8^+$ effector T-cells located randomly in the periphery similar to the distribution of the functional vascular density (Fig. 4). Also, the $CD8^+$ effector T-cells induce cancer cell cytolysis, which results in a high accumulation of dead cancer cells and a reduction of viable cancer cells as shown in Fig. 6. For the control group, the dead cancer cells are mostly in small areas where the oxygen levels are too low (i.e., necrosis due to hypoxia). Overall, anti-VEGF treatment not only reduces tumor growth during treatment but also normalizes the vascular network, which results in a more intense and uniform extravasation of immune cells, an increased amount of dead cancer cells, and a reduction in viable cancer cells. Despite the increased anti-tumor immunity that normalization treatment can induce, in the experimental data considered in our study, the immune response was not sufficient to restrict tumor growth. It seems that the immune system needs even more time to reach sufficient anti-tumor effect and thus, the anti-angiogenic treatment should be combined with targeted immunotherapies[31] and other non-targeted anti-cancer treatments to further boost anti-tumor immunity.

The activation of the adaptive immune system is also shown by the time evolution of antigen-presenting cells (APCs) and $CD8^+$ effector T-cells at the peripheral compartments as well as from their average value at the tumor compartment (Fig. 7a, b). Although initially, the APCs and $CD8^+$ effector T-cells in anti-VEGF treated tumors increase at a lower rate than in the control group, there is a point where both cell types exceed the corresponding values of the control group (Fig. 7a, b). The initial lower rate of activation of APCs and $CD8^+$ effector T-cells can be explained by the lower tumor volume and lower tumor antigen, which is caused by the delay of the angiogenesis after the anti-VEGF treatment. At longer times, the activation of APCs and $CD8^+$ effector T-cells increases due to improved tumor perfusion caused by the normalization of the vasculature (anti-VEGF treatment), which in turn causes a higher and more uniform extravasation of immune cells inside the tumor compartment. Also, the amount of pro-inflammatory cytokines is increased with anti-VEGF treatment, whereas the

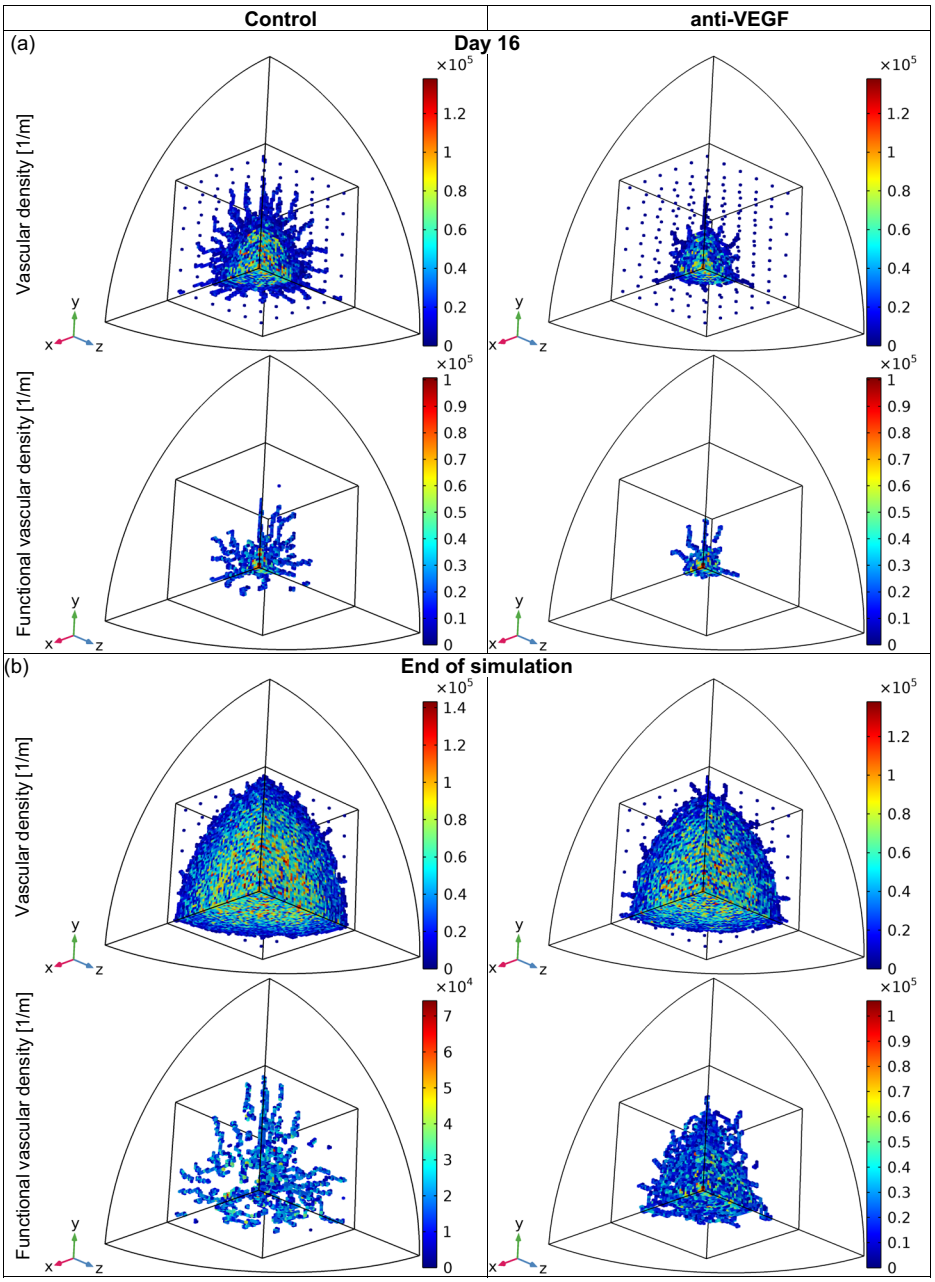

Fig. 4 | Impact of anti-VEGF treatment on the spatial distribution of neo-vessel vascular density. The spatial distribution of the vascular density and functional vascular density of neo-vessels after treatment for control and anti-VEGF on Day 16 (**a**) and at the end of the simulation (**b**).

Table 1 | Percent of functional vessels calculated for different regions of the tumor, for Control and anti-VEGF at two different time points.

	Volume of calculation	Day 16		At the end of the simulation	
		Control	anti-VEGF	Control	anti-VEGF
Percent of functional vessels	Entire tumor	21.95%	31.36%	7.66%	11.51%
	Peritumoral region	16.17%	19.75%	5.54%	2.68%
	Intratumoral region	37.54%	60.74%	9.25%	19.33%

Functional vessels are defined as vessels with average cross-sectional velocity higher than 0.1 mm/s which is sufficient to determine well-perfused vessels.

amount of anti-inflammatory cytokines is decreased which could be explained by the immunosupportive effect of vascular normalization[31].

Discussion

In this study, we formulated a comprehensive mathematical model capturing the dynamic of solid tumor growth, VEGF-driven angiogenesis, anti-angiogenic drugs, and pivotal cancer-immune-cell interactions. Our model was compared with previously published experimental data[4] and served as a tool to examine critical mechanisms influencing the effectiveness of anti-angiogenic treatment in solid tumors and their effect on the local (tumor microenvironment) and systemic immune response. The following mechanisms arise from the mathematical model and the pertinent literature[18,19,21,22] (i) anti-VEGF treatment could mitigate and temporally delay the angiogenesis, resulting in reduced tumor growth, (ii) normalization of the vasculature by reducing the permeability of the vessels and/or pruning

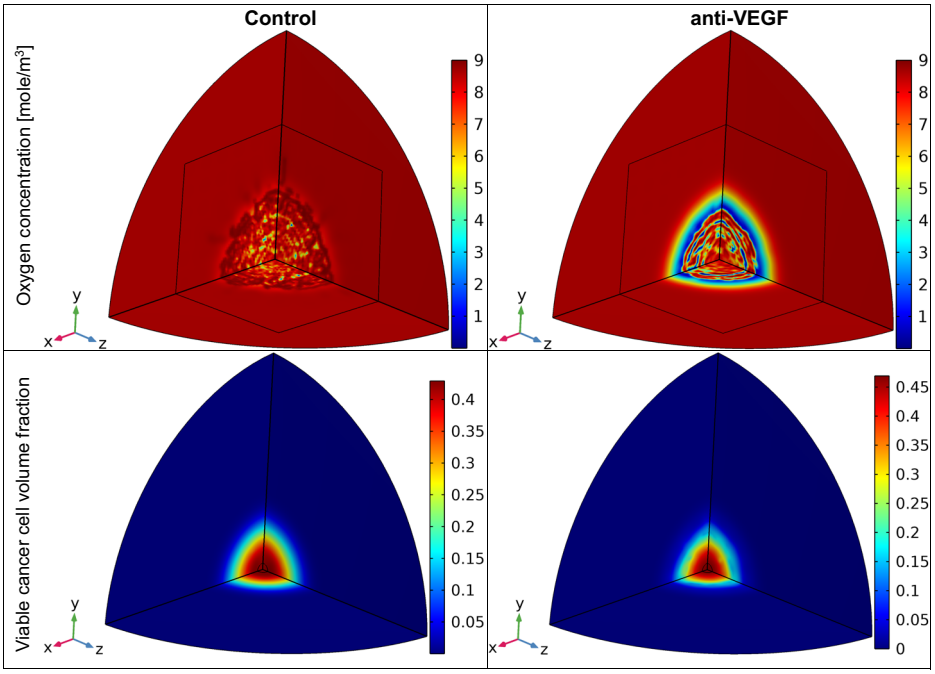

Fig. 5 | Impact of Anti-VEGF treatment on the spatial distribution of oxygen concentration and viable cancer cells. The spatial distribution of oxygen concentration [mole/m^3] and viable cancer cells (volume fraction) for control and anti-VEGF on day 16 of the simulation.

immature vessels can increase the functional vascular network with a more uniform distribution inside the tumor, (iii) vascular normalization can improve immune cells infiltration and their uniform distribution within the tumor. However, prolonged anti-VEGF treatment can cause negative outcomes because during anti-angiogenic therapy, cancer cells transition towards an invasive phenotype and migrate inside the healthy tissue, excessive vessel pruning increases the levels of hypoxia with immunosuppressive effects, and at the end of the anti-angiogenic treatment, cancer cells can rapidly proliferate inside the healthy tissue by transitioning back to a proliferative phenotype. Overall, the positive contribution of the anti-angiogenic treatment must balance the possible negative effects by choosing a proper treatment protocol.

Interestingly, we found that anti-angiogenic treatment increased the number of functional intratumoral vessels by 23% and 10% on day 16 and at the end of the simulation, respectively. The computational results indicate that the percentage of functional vessels with anti-angiogenic treatment is increased within a period that defines the normalization window[29]. The normalization window can be defined as the time interval that optimizes tumor perfusion with the use of anti-angiogenic drugs. Our mathematical model can thus be employed to provide insights into the mechanisms of vascular normalization strategies combined with targeted immunotherapies and/or other non-targeted anti-cancer treatments given that vascular normalization alone cannot boost anti-tumor immunity, whereas targeted immunotherapy alone cannot be effective due to the heterogeneity of cancer cells' antigens[23,32].

While our developed hybrid model significantly advances the understanding of complex interactions within solid tumors and the basic immune responses, it is important to acknowledge certain limitations inherent to its design and assumptions. Firstly, the model's complexity, incorporating a combination of continuous 3D tumor growth, discrete tumor-induced angiogenesis, and immune response compartments, introduces computational challenges that may limit the feasibility of extensive parametric analysis. The stochastic calculation of vessel formation in the discrete domain, while capturing the inherent randomness of angiogenesis, poses challenges in terms of computational efficiency. Furthermore, our model assumes a simplified representation of the tumor microenvironment and host tissue, overlooking potential heterogeneities that exist within a real tumor and its environment. Another possible effect of angiogenesis and anti-angiogenic treatment is the potential dynamic of acid production and variations in H^+ concentrations in the tumor. The acidic environment in the tumor can induce immunosuppression[33,34] and it should be investigated both with experiments and mathematical modeling. Mathematical modeling requires the incorporation of acid production and aerobic and anaerobic glycolysis as well as their effects on immune response, which would further increase the complexity of the current model. Additionally, the model assumes a uniform distribution of immune cells and cytokines throughout the four compartments that comprise the entire body, neglecting potential regional variations that may impact the local immune response of specific organs. These assumptions were made in order to reduce the unknown parameters for each organ/compartment. It must be noted that our model considers only one tumor antigen but in reality, the continuous mutations of tumor cells could result in more than one antigen which can affect the immune response. Despite these limitations, our model serves as a valuable tool for exploring key mechanisms influencing the effects of vascular normalization and immune response in solid tumors, offering insights that can guide further refinement and development of more sophisticated models and optimized treatment in the future.

Overall, we present here a methodology to include immune-system response to hybrid-type models composed of a discrete tumor vasculature and a continuous solid tumor growth. Our model aligns well with clinical observations, particularly in the context of anti-VEGF treatment for high-grade glioblastoma (relapsed or progressing glioblastoma). As highlighted in our study and supported by the literature[35–37], anti-VEGF therapy has demonstrated promise in prolonging survival and improving the quality of life for patients with relapsed or progressing glioblastoma. Notably, the parametric analysis in Fig. 2c, focusing on crucial mechanisms, such as the tumor growth rate and cancer cell random mobility (i.e., their invasiveness to the surrounding tissue), indicates increased efficacy of anti-VEGF treatment, especially in high-grade gliomas, with a greater volume reduction compared to less proliferate and less invasive gliomas. Furthermore, the reduction in the interstitial fluid pressure (Supplementary Fig. 2) post-anti-VEGF treatment, as indicated by our simulation results, correlates with the observed clinical outcome of reduced edema in glioblastoma patients with anti-VEGF treatment[36]. While acknowledging the challenges of directly comparing simulated interstitial fluid pressure values with clinical data due to the absence of such data in the literature[38]; the observations of the clinical trial and the model are in agreement. By considering that anti-VEGF monotherapy did not induce sufficient immune response as found in

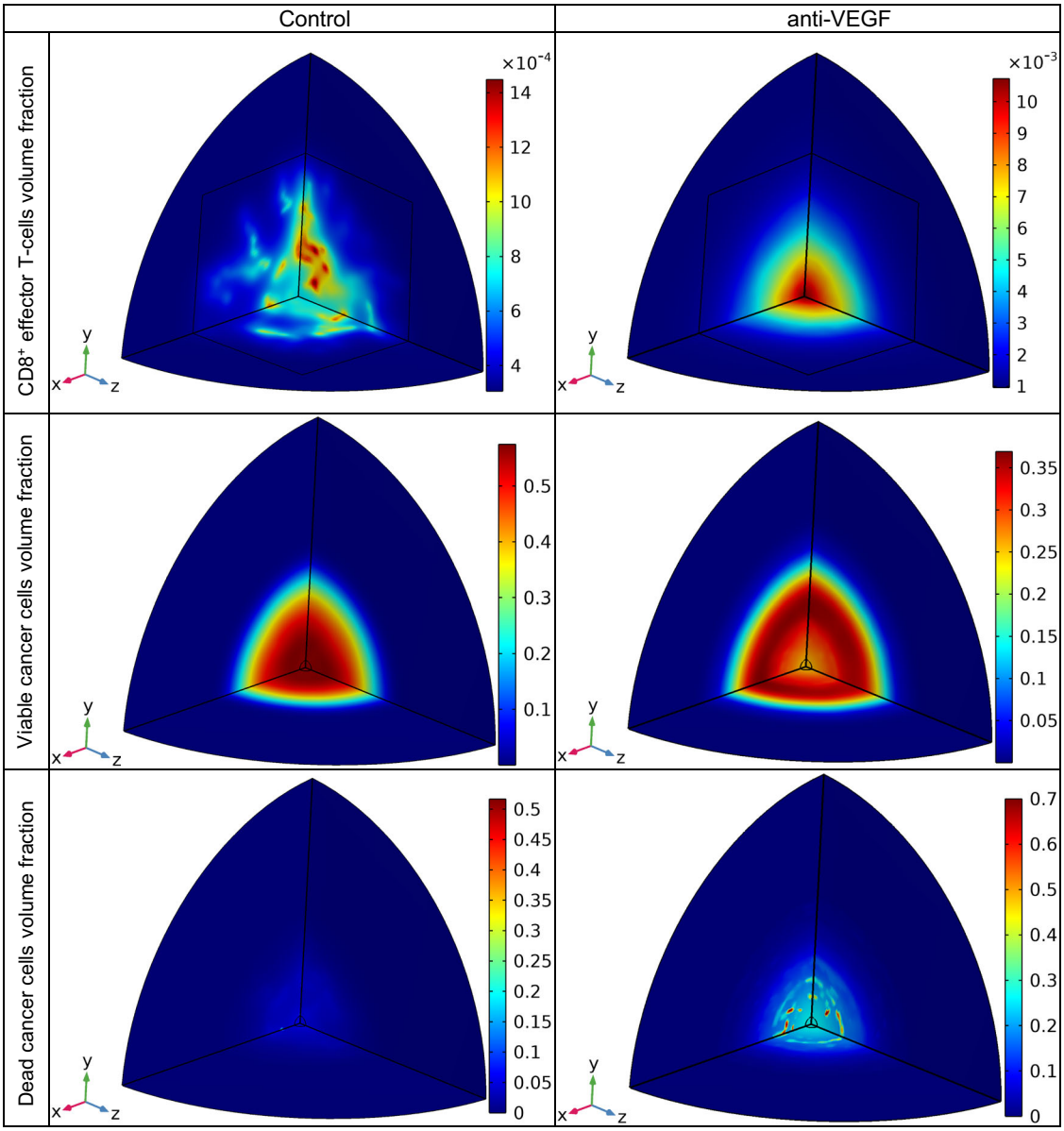

Fig. 6 | Comparison between control and anti-VEGF treatment of CD8⁺ effector T-cells, viable and dead cancer cells. The spatial distribution of CD8⁺ effector T-cells, viable and dead cancer cells volume fraction for control and anti-VEGF at the end of the simulation.

clinical trials and predicted by our model, we propose exploring combination therapies of anti-VEGF treatment with targeted immunotherapy and non-targeted anti-cancer therapies, to directly target cancer cells with known and unknown tumor antigens. Our model could be helpful in studying the underlying mechanisms of such combination therapies and provide insights for better treatment outcomes.

Methods

The model was built in COMSOL Multiphysics v5.6 (Burlington, MA) and interacts with MATLAB codes for the calculation of angiogenesis and intravascular pressure. Box 1 presents an overview of the algorithm, the interactions between MATLAB and COMSOL Multiphysics as well as the core equations. The mathematical framework, the complete set of equations, and the solution strategy are provided in detail in the Supplementary Information.

Continuous tumor domain model

In the 3D continuous tumor compartment, the solid (Φ_s) and fluid (Φ_f) phases conservation is calculated[39] as well as the volume fraction of viable cancer cells (Φ_c), dead cancer cells (Φ_d), CD8⁺ effector T-cells (Φ_{T^E}), antigen-presenting cells (Φ_{APC}) and dendritic cells (Φ_{DC}). The conservation of all cells in the tumor compartment was calculated as solid phases by considering their accumulation, convection with solid velocity ($\mathbf{v}_s$) in the conservative form to satisfy the volume change, diffusion, and reaction (the reaction terms are given in Supplementary Table 3); see Box 1 conservation of solid phases. The mechanical stress is also calculated by decomposition of the deformation gradient tensor ($\mathbf{F}$) in elastic deformation ($\mathbf{F}_e$) and inelastic deformation due to tumor growth (growth deformation gradient tensor, $\mathbf{F}_g$)[12,40–42]. The inelastic growth deformation gradient tensor was calculated by the growth stretch ratio (λ_g). The growth stretch ratio depends on the total accumulation of the solid phase (i.e., viable minus dead cancer cells). The 2nd Piola-Kirchhoff stress tensor was calculated using the constitutive equation of the Neo-Hookean material and solving for the momentum balance; see equations in Box 1 and section "Solid mechanics—mechanical stress in tumor compartment" in Supplementary information for more details. The interstitial fluid pressure (p) is also calculated by Darcy's equation and the conservation of medium (solid and fluid phases), which considers the fluid supply by blood vessels (pre-existing and neo-vessels)

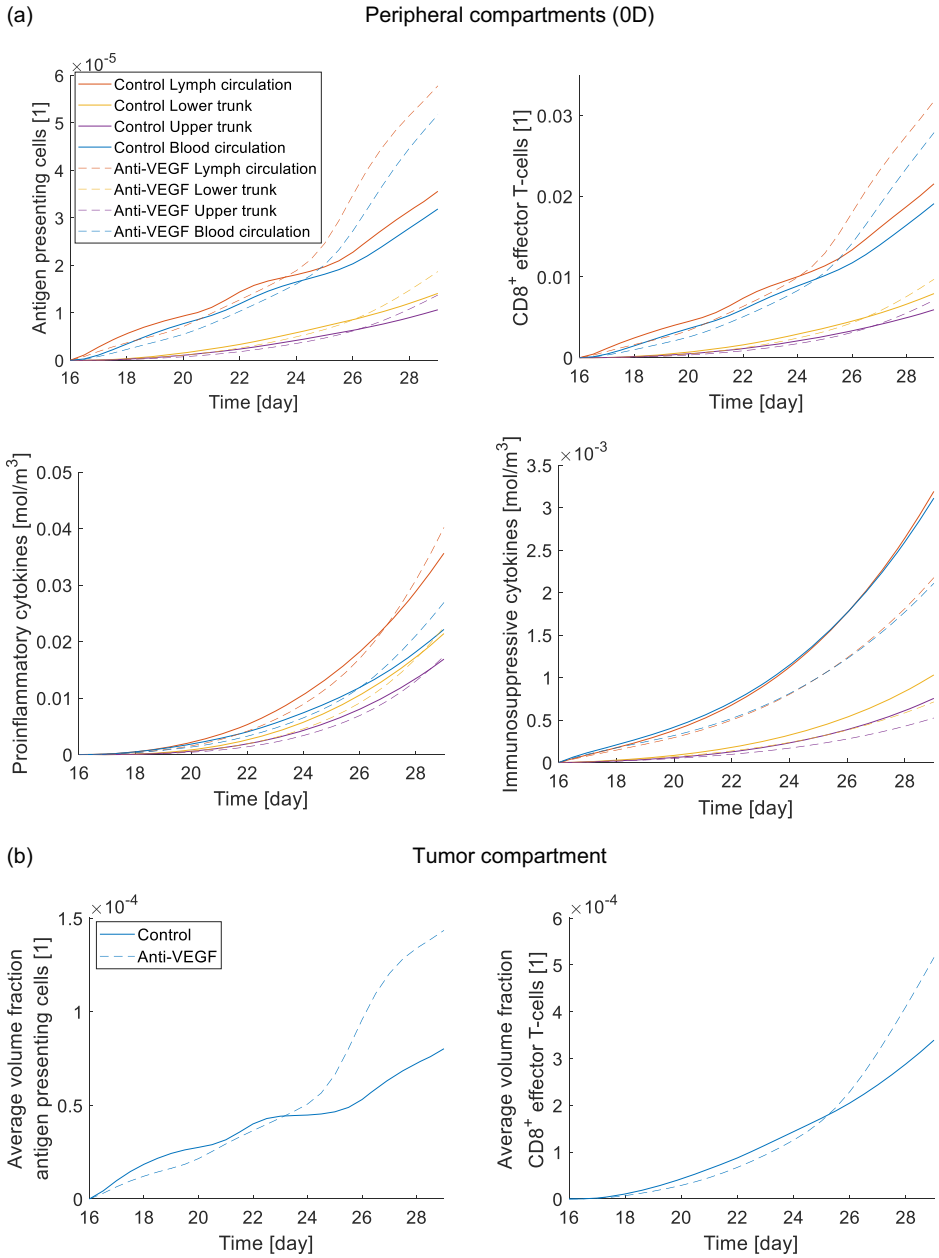

Fig. 7 | Temporal dynamic of immune cells and cytokine under control and anti-VEGF treatment. The time evolution of antigen-presenting cells, $CD8^+$ effector T-cells, pro- and anti-inflammatory cytokines: **a** in the peripheral compartments (upper and lower trunk, lymph, and blood circulations) and **b** the tumor compartment for the control versus anti-VEGF treatment.

and the fluid absorption by the lymphatic vessels; see conservation of medium in Box 1 and section "Conservation of solid and fluid-phase in the tumor compartment" in Supplementary information for more details. The mass balance of oxygen (c_{ox}), cytokines pro-inflammatory (c_p) and immunosuppressive (c_a), and angiogenic factors VEGF (c_{VEGF}) are solved as diluted species; see conservation of diluted species in Box 1. The conservation of diluted species was calculated by considering their accumulation, convection with average bulk velocity ($\mathbf{v}_{ab}$) in conservative form to satisfy the volume change, diffusion, and reaction; the reaction terms of these species are given in Supplementary Table 4. Matrix metalloproteinases (c_{MMPs}) and fibronectin a part of the extracellular matrix (c_{EXM}) are also calculated (their equations are given in the section "Mass balance of diluted species in the tumor compartment" of Supplementary information).

Discrete model of tumor-induced angiogenesis

The process of angiogenesis is initiated to satisfy the increased demand for oxygen by the cancer cells. The motion of discrete vessels is calculated stochastically in the 3D discrete model in MATLAB with probabilities $P_0 - P_6$. The tips of the vessels have random mobility, a motion due to the gradient of soluble angiogenic factors, such as VEGF (chemotaxis), and a motion in response to the gradient of bound molecules within the extracellular matrix (haptotaxis). All these mechanisms define the values of the probabilities $P_0 - P_6$[8,9,43]. The probabilities and the motion of discrete vessels are calculated in the 3D discrete model whereas the VEGF and extracellular matrix values are calculated in the 3D continuous model (COMSOL Multiphysics) and transferred to the 3D discrete model (Box 1). For more information see the section "Discrete mathematical model of endothelial cells motion (angiogenesis) in tumor compartment" in Supplementary information. The vascular density (Sv) and functional vascular density (Sv_f) are transferred in the 3D continuous model. The vascular densities (Sv and Sv_f) are calculated by adding the pre-existing vascular density and the total surface of discrete vessels inside the volume of a tissue element divided by this volume (see Box 1). Only discrete vessels with an average velocity higher than 0.1 mm/s contribute to the functional vascular density[28,44]. For the discrete neo-vessels, the volumetric fluid flow rate in each vessel and transvascular fluid flow rate into interstitial space are also calculated by

Box 1 | Overview of the hybrid mathematical model and core equations (solid mechanics and conservation of mass). Curved arrows illustrate the interactions and information transfer between the 3D discrete and 3D continuous models. (cell images were adapted from BioRender.com)

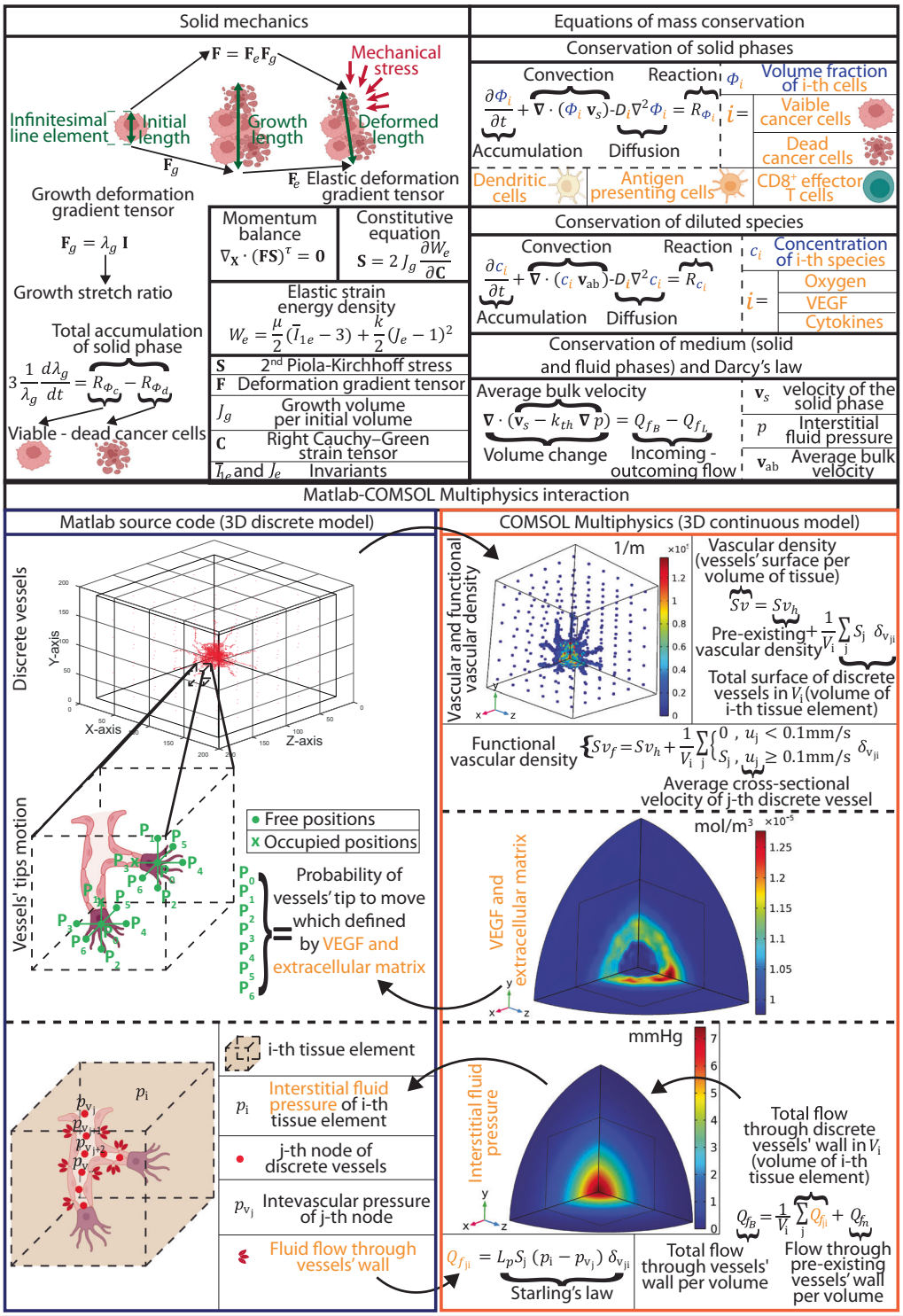

considering the mass balance of fluid. All these quantities depend on both the vascular fluid pressure (p_v) and interstitial fluid pressure (p). The vascular pressure (p_{vj}) was calculated for each j-th discrete vessel node as it is presented in Box 1. The fluid flow through vessels' walls is calculated by Starling's approximation by using the p_{vj} and p which are calculated in the 3D discrete model and 3D continuous model, respectively[12]. The coupling of all these quantities was satisfied by transferring the total flow across the vessels' wall in the 3D continuous model, which contributes to the calculation of the interstitial fluid pressure and then the fluid pressure is transferred back to the 3D discrete model, see the schematic representation in Box 1 and for more information see section "Calculation of volumetric fluid flow rate in vessels and transvascular fluid flow rate into interstitial space of the tumor compartment" in Supplementary information. The calculation of flow through vessels allows the calculation of vessels' average cross-sectional velocity and subsequently the functional vascular density which is used to calculate the infiltration of the immune cells into the tumor compartment. It must be noted that the diluted species like oxygen supply depends on the vascular density (not the functional vascular density) because the oxygen is a small molecule and can be transported by diffusion without the need for sufficient perfusion like immune cells.

Modeling of transport of cells and cytokines between compartments

The body of the mouse is divided into compartments, and they are connected as presented in Fig. 1 and Supplementary Fig. 3. All the immune cells ($CD8^+$ effector T-cells, antigen-presenting cells, and dendritic cells) and the pro-inflammatory and immunosuppressive cytokines are transported through the different compartments. The mass balance for all these variables in the 0D compartments is given by the following equation:

$$V_c \frac{\partial y_c}{\partial t} = \sum Q_j^{in} y_j^{in} - \sum Q_i^{out} y_c - V_c \sum R_{y_c} - \int\int\int_{V_T} T_{y_c} \quad (1)$$

Where the first term is the accumulation of each quantity in each 0D compartment, the second term is the incoming quantity from other 0D compartments, the third term is the outcoming quantity to other 0D compartments, the fourth term describes the reactions that take place inside the 0D compartments and the final term connects the blood and lymph circulations (0D compartments) with the 3D tumor compartment by integrating the exchange of mass from 0D compartments to the 3D tumor compartment[44]. The incoming and outcoming volumetric flows and the volume of each compartment are given in Supplementary Table 5. For more details see the section "Immune cells and cytokines transport through pharmacokinetic/pharmacodynamic compartments" of the Supplementary information. Their reaction terms (R_{y_c}) as well as the mass transported in and out of the tumor compartment (T_{y_c}) are defined in Supplementary Table 6.

Data availability

The experimental data of the pre-clinical study are available in ref. 4. The full raw dataset of this article is provided as a supplementary file (Supplementary raw data).

Code availability

The COMSOL Multiphysics model is available online as a MATLAB script (https://doi.org/10.5281/zenodo.11207573).

Received: 30 January 2024; Accepted: 31 July 2024;
Published online: 02 December 2024

References

1. Stylianopoulos, T., Munn, L. L. & Jain, R. K. Reengineering the physical microenvironment of tumors to improve drug delivery and efficacy: from mathematical modeling to bench to bedside. *Trend Cancer* **4**, 292–319 (2018).
2. Munn, L. L. & Jain, R. K. Vascular regulation of antitumor immunity. *Science* **365**, 544–545. (2019).
3. Jin, M. Z. & Jin, W. L. The updated landscape of tumor microenvironment and drug repurposing. *Signal. Transduct. Target. Ther.* **5**, 1–16 (2020).
4. Dong, X. et al. Anti-VEGF therapy improves EGFR-vIII-CAR-T cell delivery and efficacy in syngeneic glioblastoma models in mice. *J. Immunother. Cancer* **11**, e005583 (2023).
5. Deng, C. et al. The vascular disrupting agent CA4P improves the antitumor efficacy of CAR-T cells in preclinical models of solid human tumors. *Mol. Ther.* **28**, 75–88 (2020).
6. Shrimali, R. K. et al. Antiangiogenic agents can increase lymphocyte infiltration into tumor and enhance the effectiveness of adoptive immunotherapy of cancer. *Cancer Res.* **70**, 6171–6180 (2010).
7. Baish, J. W., Netti, P. A. & Jain, R. K. Transmural coupling of fluid flow in microcirculatory network and interstitium in tumors. *Microvasc. Res.* **53**, 128–141 (1997).
8. Anderson, A. R. A. & Chaplain, M. A. J. Continuous and discrete mathematical models of tumor-induced angiogenesis. *Bull. Math. Biol.* **60**, 857–899 (1998). *1998 60:5*.
9. Wu, J. et al. Coupled modeling of blood perfusion in intravascular, interstitial spaces in tumor microvasculature. *J. Biomech.* **41**, 996–1004 (2008).
10. Cai, Y., Xu, S., Wu, J. & Long, Q. Coupled modelling of tumour angiogenesis, tumour growth and blood perfusion. *J. Theor. Biol.* **279**, 90–101 (2011).
11. Stylianopoulos, T., Soteriou, K., Fukumura, D. & Jain, R. K. Cationic nanoparticles have superior transvascular flux into solid tumors: Insights from a mathematical model. *Ann. Biomed. Eng.* **41**, 68–77 (2013).
12. Stylianopoulos, T. & Jain, R. K. Combining two strategies to improve perfusion and drug delivery in solid tumors. *Proc. Natl Acad. Sci. USA* **110**, 18632–18637 (2013).
13. Stylianopoulos, T., Economides, E. A., Baish, J. W., Fukumura, D. & Jain, R. K. Towards optimal design of cancer nanomedicines: multi-stage nanoparticles for the treatment of solid tumors. *Ann. Biomed. Eng.* **43**, 2291–2300 (2015).
14. Chauhan, V. P. et al. Normalization of tumour blood vessels improves the delivery of nanomedicines in a size-dependent manner. *Nat. Nanotechnol.* **7**, 383–388 (2012).
15. Vavourakis, V. et al. A validated multiscale in-silico model for mechano-sensitive tumour angiogenesis and growth. *PLoS Comput. Biol.* **13**, e1005259 (2017).
16. Vavourakis, V., Stylianopoulos, T. & Wijeratne, P. A. In-silico dynamic analysis of cytotoxic drug administration to solid tumours: effect of binding affinity and vessel permeability. *PLoS Comput. Biol.* **14**, e1006460 (2018).
17. Arvanitis, C. D. et al. Mechanisms of enhanced drug delivery in brain metastases with focused ultrasound-induced blood–tumor barrier disruption. *Proc. Natl Acad. Sci. USA* **115**, E8717–E8726 (2018).
18. Martin, J. D., Seano, G. & Jain, R. K. Normalizing function of tumor vessels: progress, opportunities, and challenges. *Annu. Rev. Physiol.* **81**, 505–534 (2019).
19. Carmeliet, P. & Jain, R. K. Principles and mechanisms of vessel normalization for cancer and other angiogenic diseases. *Nat. Rev. Drug Discov.* **10**, 417–427 (2011).
20. Wang, N., Jain, R. K. & Batchelor, T. T. New directions in anti-angiogenic therapy for glioblastoma. *Neurotherapeutics* **14**, 321–332 (2017).
21. Winkler, F. et al. Kinetics of vascular normalization by VEGFR2 blockade governs brain tumor response to radiation: role of oxygenation, angiopoietin-1, and matrix metalloproteinases. *Cancer Cell* **6**, 553–563 (2004).

22. Peterson, T. E. et al. Dual inhibition of Ang-2 and VEGF receptors normalizes tumor vasculature and prolongs survival in glioblastoma by altering macrophages. *Proc. Natl Acad. Sci. USA* **113**, 4470–4475 (2016).
23. Wang, H. et al. The challenges and the promise of molecular targeted therapy in malignant gliomas. *Neoplasia* **17**, 239–255 (2015).
24. Drevelegas, A. & Karkavelas, G. High-Grade Gliomas. in *Imaging of Brain Tumors with Histological Correlations* (ed. Drevelegas, A.) 109–135 (Springer Berlin Heidelberg, 2002).
25. Kim, H. J. et al. CREB5 promotes the proliferation and self-renewal ability of glioma stem cells. *Cell Death Discov.* **10**, 1–8 (2024).
26. Hatzikirou, H., Basanta, D., Simon, M., Schaller, K. & Deutsch, A. 'Go or Grow': the key to the emergence of invasion in tumour progression? *Math. Med. Biol.* **29**, 49–65 (2012).
27. Xie, Q., Mittal, S. & Berens, M. E. Targeting adaptive glioblastoma: an overview of proliferation and invasion. *Neuro Oncol.* **16**, 1575–1584 (2014).
28. Kamoun, W. S. et al. Simultaneous measurement of RBC velocity, flux, hematocrit and shear rate in vascular networks. *Nat. Methods* **7**, 655–660 (2010).
29. Huang, Y., Stylianopoulos, T., Duda, D. G., Fukumura, D. & Jain, R. K. Benefits of vascular normalization are dose and time dependent - Letter. *Cancer Res.* **73**, 7144–7146 (2013).
30. Mascheroni, P. et al. On the impact of chemo-mechanically induced phenotypic transitions in gliomas. *Cancers* **11**, 716 (2019).
31. Fukumura, D., Kloepper, J., Amoozgar, Z., Duda, D. G. & Jain, R. K. Enhancing cancer immunotherapy using antiangiogenics: opportunities and challenges. *Nat. Rev. Clin. Oncol.* **15**, 325 (2018).
32. Touat, M., Idbaih, A., Sanson, M. & Ligon, K. L. Glioblastoma targeted therapy: updated approaches from recent biological insights. *Ann. Oncol.* **28**, 1457–1472 (2017).
33. Boedtkjer, E. & Pedersen, S. F. The acidic tumor microenvironment as a driver of cancer. *Annu. Rev. Physiol.* **82**, 103–126 (2020).
34. Huber, V. et al. Cancer acidity: an ultimate frontier of tumor immune escape and a novel target of immunomodulation. *Semin. Cancer Biol.* **43**, 74–89 (2017).
35. Chinot, O. L. et al. Bevacizumab plus radiotherapy–temozolomide for newly diagnosed glioblastoma. *N. Engl. J. Med.* **370**, 709–722 (2014).
36. Friedman, H. S. et al. Bevacizumab alone and in combination with irinotecan in recurrent glioblastoma. *J. Clin. Oncol.* **27**, 4733–4740 (2009).
37. Garcia, J. et al. Bevacizumab (Avastin®) in cancer treatment: a review of 15 years of clinical experience and future outlook. *Cancer Treat. Rev.* **86**, 102017 (2020).
38. Boucher, Y., Salehi, H., Witwer, B., Harsh, G. R. & Jain, R. K. Interstitial fluid pressure in intracranial tumours in patients and in rodents. *Br. J. Cancer* **75**, 829–836 (1997).
39. Roose, T., Netti, P. A., Munn, L. L., Boucher, Y. & Jain, R. K. Solid stress generated by spheroid growth estimated using a linear poroelasticity model. *Microvasc. Res.* **66**, 204–212 (2003).
40. Ambrosi, D. & Mollica, F. On the mechanics of a growing tumor. *Int. J. Eng. Sci.* **40**, 1297–1316 (2002).
41. Hadjigeorgiou, A. G. & Stylianopoulos, T. Evaluation of growth-induced, mechanical stress in solid tumors and spatial association with extracellular matrix content. *Biomech. Model Mechanobiol.* **22**, 1625–1643 (2023).
42. Voutouri, C. & Stylianopoulos, T. Accumulation of mechanical forces in tumors is related to hyaluronan content and tissue stiffness. *PLoS One* **13**, e0193801 (2018).
43. Anderson, A. R. A., Chaplain, M. A. J. & McDougall, S. In *Modeling Tumor Vasculature: Molecular, Cellular, and Tissue Level Aspects and Implications.* 9781461400523, 105–133 (Springer, 2012).
44. Zhu, H., Melder, R. J., Baxter, L. T. & Jain, R. K. Physiologically based kinetic model of effector cell biodistribution in mammals: implications for adoptive immunotherapy. *Cancer Res* **56**, 3771–81 (1996).

Acknowledgements

We acknowledge Dr. Rakesh K. Jain for providing us with the experimental data and valuable thoughts and comments for the article. This project has received funding from the European Research Council (ERC) under the European Union's Horizon 2020 research and innovation program (grant agreement no. 863955) to T.S.

Author contributions

A.G.H. and T.S. designed research; A.G.H. performed research; T.S. contributed analytic tools; A.G.H. and T.S. analyzed data; T.S. supervised the project; and A.G.H. and T.S. wrote the paper.

Competing interests

The authors declare no competing interests.

Additional information

Supplementary information The online version contains supplementary material available at https://doi.org/10.1038/s44341-024-00002-2.

Correspondence and requests for materials should be addressed to Triantafyllos Stylianopoulos.